J Low Temp Phys (2018) 193:231–240
https://doi.org/10.1007/s10909-018-1898-z

Effects of Normal Metal Features on Superconducting Transition-Edge Sensors

N. A. Wakeham[1,2] · J. S. Adams[1,3] · S. R. Bandler[1] · J. A. Chervenak[1] · A. M. Datesman[1,4] · M. E. Eckart[1] · F. M. Finkbeiner[1,5] · R. L. Kelley[1] · C. A. Kilbourne[1] · A. R. Miniussi[1,3] · F. S. Porter[1] · J. E. Sadleir[1] · K. Sakai[1,3] · S. J. Smith[1,3] · E. J. Wassell[1,4] · W. Yoon[1,2]

Received: 30 October 2017 / Accepted: 26 March 2018 / Published online: 2 April 2018

Abstract In transition-edge sensors (TESs), the addition of normal metal stripes on top of the superconducting bilayer, perpendicular to the current direction, is known to globally alter the sensitivity of the resistance R to changes in temperature T and current I. Here, we describe measurements of the dependence of the TES current on magnetic field B, bath temperature and voltage bias in devices with various numbers of stripes. We show that the normal metal features have a profound effect on the appearance of localized regions of very large $(T/R)\,\mathrm{d}R/\mathrm{d}T$. We associate this with changes in the current distribution and corresponding changes in the oscillatory pattern of $I(B)$. 140 μm TESs with no stripes are found to have a relatively smooth resistive transition and sufficiently low noise that the measured energy resolution is 1.6 eV for X-rays of 1.5 keV. The predicted energy resolution at 6 keV is better than 2 eV, once the heat capacity is optimized for these higher energies.

Keywords Transition-edge sensor · X-IFU · X-ray microcalorimeter

✉ N. A. Wakeham
nicholas.a.wakeham@nasa.gov

1 Goddard Space Flight Center (GSFC), NASA, Greenbelt, MD 20771, USA

2 NPP - Universities Space Research Association, 7178 Columbia Gateway Dr, Columbia, MD 21046, USA

3 CRESST II - University of Maryland Baltimore County, 1000 Hilltop Cir, Baltimore, MD 21250, USA

4 SGT, Inc, 7701 Greenbelt Rd, Greenbelt, MD 20770, USA

5 Wyle Information Systems, 22309 Exploration Dr, Lexington Park, MD 20653, USA

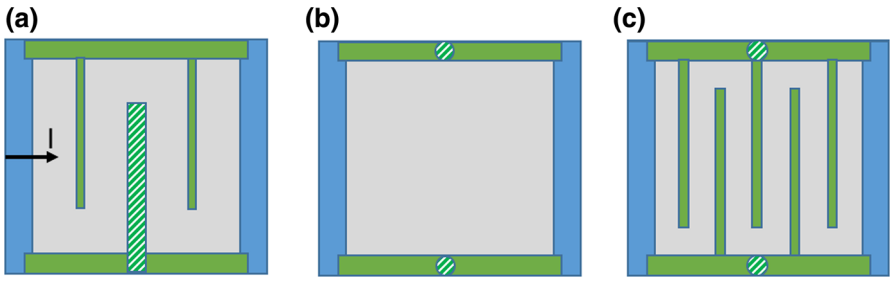

Fig. 1 Schematic diagram of TES devices viewed from above. Absorbers are not shown for clarity. Mo/Au bilayer is shown in gray, Nb leads in blue, Au absorber attachments (hatched) and Au metal features (solid) are shown in green. Arrow shows direction of current I. **a** Typical NASA/GSFC 3-stripe T-Stem device with banks and 3 metal stripes, the center one forming the T-stem absorber attachment. **b** No-stripe device with Au banks but no stripes. **c** 5-stripe device with five Au stripes across the TES (Color figure online)

1 Introduction

Superconducting transition-edge sensors (TESs) are the baseline detector technology for the X-ray Integral Field Unit on the Advanced Telescope for High-Energy Astrophysics (Athena) mission [1]. This type of astronomical application requires a large array of TES microcalorimeter pixels with highly uniform spectral performance. Achieving this will require minimizing the sensitivity of the spectral performance of each TES to small changes in parameters such as applied perpendicular magnetic field B, bath temperature $T_{\rm bath}$, applied voltage V, and TES current I. TES devices fabricated at NASA/GSFC typically have isolated regions of this parameter space where the derivative of the resistance R with respect to I and the temperature of the TES T, is very large [2]. These so-called kinks are associated with a large magnitude of the electrical noise exceeding theoretical expectations (unexplained noise) that is commonly observed in TESs [4,5], and degraded spectral performance. In addition, the presence of these regions may make achieving the energy gain scale calibration requirements for Athena [3] extremely challenging. Therefore, it is important to understand the origin of these kinks and how we might exclude them from our desired parameter space.

A schematic diagram of a typical NASA/GSFC TES is shown in Fig. 1a. The 140 μm square Mo/Au superconducting bilayer is electrically connected with Nb leads. In addition, Au banks are placed down the edges of the TES parallel to the current direction and Au is also added in two stripes perpendicular to the current direction as shown. A third stripe of Au is then formed by the T-stem attachment to the absorber. There is evidence that the addition of the normal metal stripes is correlated with a reduction in the unexplained noise [4,5]. However, these 3-striped devices have been measured and predicted to have complex $R(I, T, B)$ surfaces including kinks [2,6]. An important outstanding question is whether the stripe patterns may be optimized to control the kinks in the transition while maintaining the excellent spectral performance achieved in the traditional devices when operated in regions of parameter space without kinks [7].

In this report, we describe measurements of three TES designs, shown in Fig. 1, fabricated onto a single chip. There is a traditional 3-stripe T-stem device, described above, and a no-stripe device that has Au banks, no additional Au stripes, and the

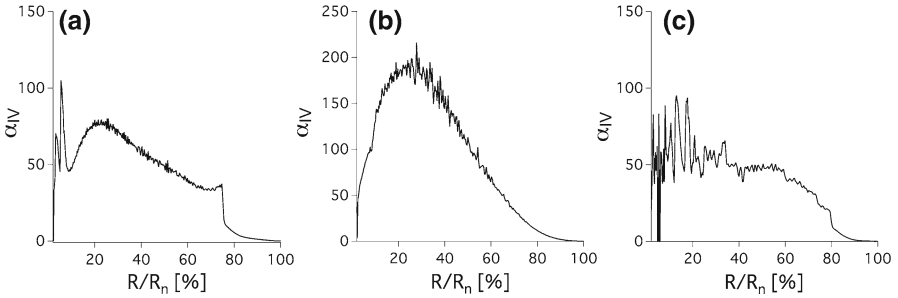

Fig. 2 $\alpha_{IV} = (T/R)\mathrm{d}R/\mathrm{d}T$ as a function of R/R_n calculated from measurement of $I(V)$ at $T_{\mathrm{bath}} = 55$ mK for a **a** 3 stripe T-stem, **b** no-stripe, and **c** 5-stripe device

absorber is attached to the TES at small circular dot stems on each of the banks. Finally, there is a 5-stripe device that has five Au stripes equally spaced across the TES and also has dot stems on the banks. The sheet resistance of the Mo/Au bilayer was 14 m$\Omega/\square$. Section 2 describes measurements of the effects of the stripes on $R(I, T, B)$, showing the favorability of the no-stripe device in terms of this resistive surface. Section 3 then discusses the spectral and noise performance of these no-stripe devices.

2 Effect of Metal Stripes on $R(I, T, B)$

Measurements of $I(V)$ were taken on TESs with the three different stripe patterns shown in Fig. 1. The experimental setup is described in detail in reference [2]. The thermal conductance $G(T)$ of the TES to the thermal bath was calculated from measurements of $I(V)$ taken at different bath temperatures [8]. $R(T)$ was then calculated using the measured $G(T)$ and measurements of $I(V)$ at $T_{\mathrm{bath}} = 55$ mK [8]. The normalized derivative of this $R(T)$ curve, $\alpha_{IV} = (T/R)\mathrm{d}R/\mathrm{d}T$, for each stripe design is shown in Fig. 2. For the 3-stripe device, the typical kinks in the transition are seen in Fig. 2a as two clear spikes in α_{IV} below 15% of the normal state resistance R_n. Note that although features in α_{IV} are always observed in the NASA/GFSC 3-stripe devices, the exact value of R/R_n and the precise shape of the kinks may vary depending on G, T_{c}, B etc. In the 5-stripe design, there are several dramatic kinks throughout the transition, but in the no-stripe design the transition is smooth with only a very small feature at a bias around 10% R_n.

To study the origin and dependencies of these kinks in more detail, we apply a constant V to the TES, and measure I as B is varied using a wire coil above the TES. Figure 3a shows $I(B)$ taken at $T_{\mathrm{bath}} = 55$ mK on the 3-stripe T-stem device at various values of V. The general oscillatory pattern is related to the TES acting as a weak link and the applied magnetic field causing a phase winding of the order parameter, as discussed in detail elsewhere [2,6,9,10]. The asymmetry in the pattern about $B = 0$ is a consequence of the magnetic 'self-field' induced from the current in the TES and electrical bias leads. In addition to the general oscillatory pattern, at small V, we observe regions where there is a dramatic change in $\mathrm{d}I/\mathrm{d}B$ at a local maximum in $I(B)$. The black circles on Fig. 3a indicate these regions in the field range

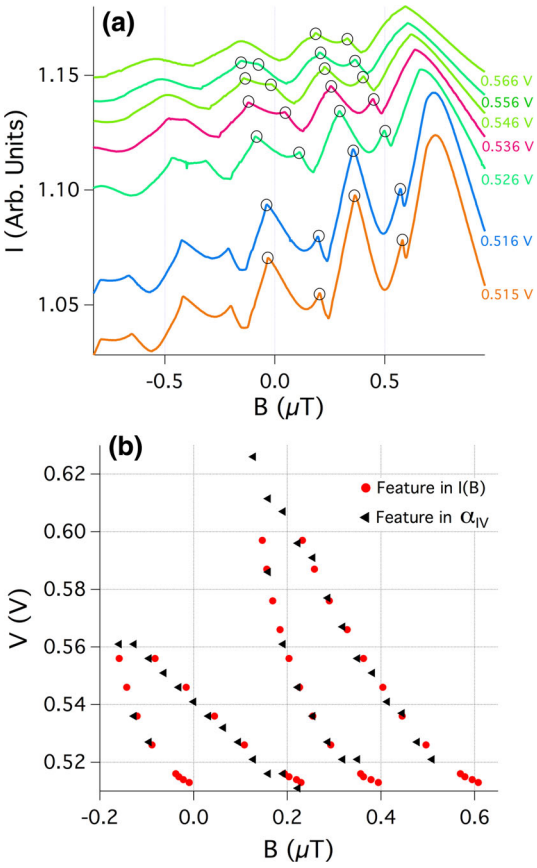

Fig. 3 **a** $I(B)$ for the 3-stripe T-stem device at indicated values of V and $T_{\text{bath}} = 55$ mK . Curves are arbitrarily offset vertically for clarity. **b** V and B at which a rapid change in $\mathrm{d}I/\mathrm{d}B$ is observed , circled in (**a**), (red circle), and a sharp spike or feature is observed in the $\alpha_{IV} = (T/R)\mathrm{d}R/\mathrm{d}T$ (black triangle) (Color figure online)

-0.2 to 0.6 μT as V was varied. To understand whether these regions are related to the kinks observed in the $R(T)$, measurements of $I(V)$ were taken at different fixed B over this same field range. Figure 3b shows B and V values at which the kinks are observed in these α_{IV} measurements. In addition, Fig. 3b shows the values of B and V of the regions with a large change in $\mathrm{d}I/\mathrm{d}B$ in measurements of $I(B)$ at constant V. This figure shows that these features in the two measurements are approximately coincident, and therefore, we may associate the circled regions of $I(B)$ with the kinks in $R(T)$ and α_{IV}.

Figure 4a shows $I(B)$ for the 5-stripe and no-stripe devices at $T_{\text{bath}} = 55$ mK and constant V such that $R/R_n \approx 10\%$ at $B = 0$. In the no-stripe device, the magnitude of the change in I over the full field range is relatively large but the change is smooth. In the 5-stripe device, the total magnitude of the change in I is small, but there are many regions where $\mathrm{d}I/\mathrm{d}B$ changes rapidly, consistent with the many spikes observed in α_{IV}.

To understand the stark difference in $I(B)$ at $T_{\text{bath}} = 55$ mK between the 5-stripe and no-stripe devices, we now compare $I(B)$ at T_{bath} close to T_c for each device. This is shown in Fig. 4b for constant V such that $R/R_n \approx 5\%$ at $B = 0$.

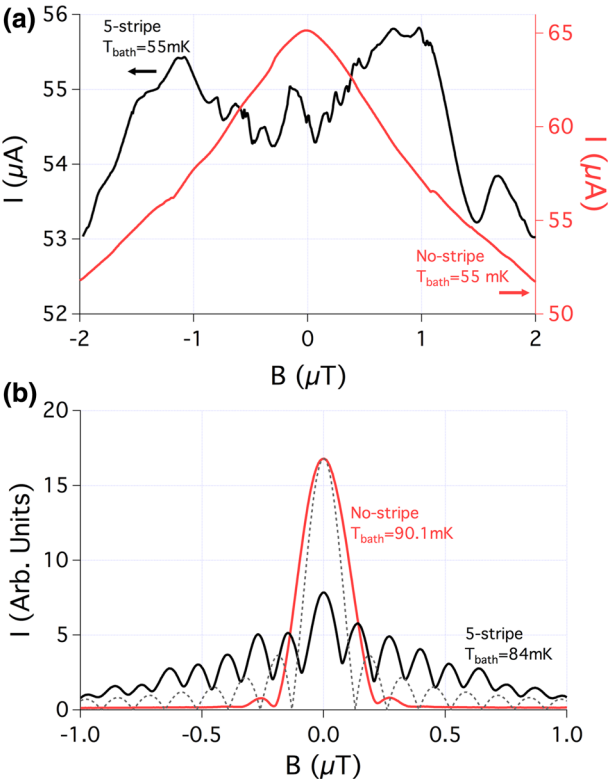

Fig. 4 **a** $I(B)$ for a 5-stripe device (black) and a no-stripe device (red) at constant V (corresponding to $R/R_n \approx 10\%$ at $B = 0$) and $T_{\text{bath}} = 55$ mK. **b** $I(B)$ at T_{bath} just below T_c for the 5-stripe device (black, $T_c = 84.5$ mK) and a no-stripe device (red, $T_c = 91.7$ mK) at constant V (corresponding to $R/R_n \approx 5\%$ at $B = 0$). Dashed line shows predicted Josephson–Fraunhofer pattern for $I_c(B)$ for a uniform current distribution across a weak link of equal area to a 140 μm TES [6] (Color figure online)

Close to T_c, the oscillatory pattern of $I(B)$ has a more Fraunhofer-type pattern. The key features in this pattern are the width and height of the central maximum relative to the period and amplitude of the subsequent oscillations at field magnitudes outside of the central maximum. The predicted oscillatory pattern in the critical current $I_c(B)$ in the simplest treatment of a Josephson junction is proportional to the magnitude of the Fourier transform of the current distribution. For example, in the limit of a uniform current distribution across the junction one expects the Fraunhofer pattern, where the central maximum is $3\pi/2$ times larger than the subsequent maximum and twice as wide as all other maxima. In the limit of a current distribution that is a delta function at each edge of the junction, one expects the SQUID-type response where the central maximum is equal height and width to all other maxima [11].

The pattern shown for the no-stripe device in Fig. 4b is consistent with previous observations of $I_c(B)$ of no-stripe devices [6]. The central maximum has a larger amplitude and width than predictions for a uniform current distribution across the

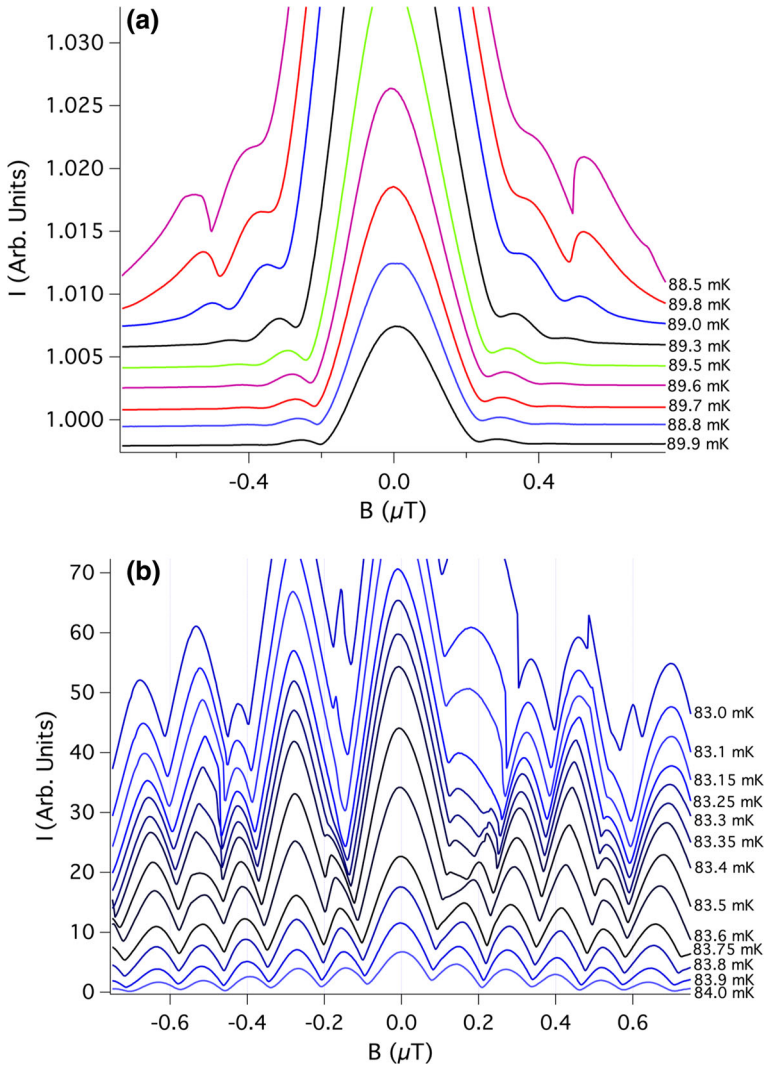

Fig. 5 $I(B)$ for the **a** no-stripe device and **b** 5-stripe device at indicated values of T_{bath} and at constant V (corresponding to $R/R_n \approx 5\%$ at $B = 0$). Curves are arbitrarily offset vertically for clarity (Color figure online)

weak link of the TES. The oscillation period B_p is consistent with expectations for a weak link with $B_p = \Phi_0/A$, where A is the area of the TES, and Φ_0 is a flux quantum. Therefore, the oscillatory pattern observed in the no-stripe device is consistent with a supercurrent density distribution perpendicular to the current direction that is smallest at the edges of the TES and largest in the center. This is qualitatively consistent with expectations that close to the normal metal banks superconductivity is suppressed by the proximity effect [6,12]. The measurement of $I(B)$ close to T_c in the 5-stripe device shows very different behavior. The central maximum has a small amplitude and width

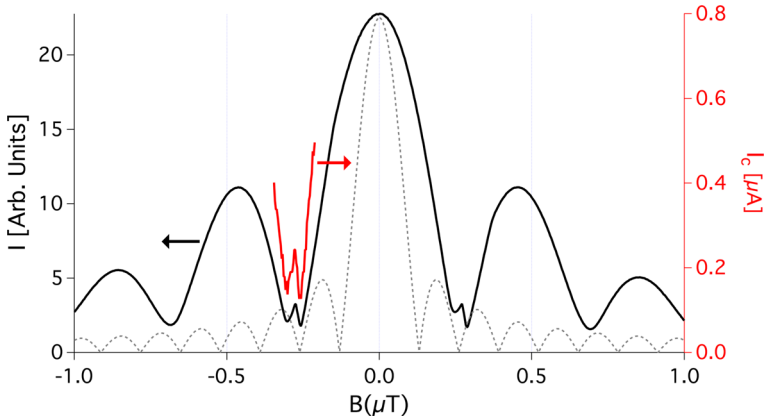

Fig. 6 $I(B)$ (black) and $I_c(B)$ (red) for 3-stripe device at $T_{bath} = 86.8$ mK ($T_c = 87.6$ mK) and constant V (corresponding to $R/R_n \approx 5\%$ at $B = 0$). Dashed line shows predicted Josephson–Fraunhofer pattern for $I_c(B)$ for a uniform current distribution across a weak link of equal area to a 140 μm TES (Color figure online)

relative to expectations for a uniform current distribution. This can be interpreted as the supercurrent density being largest toward the edges of the TES and smallest at the center. This suggests that when the spacing between normal metal stripes is sufficiently small, superconductivity is suppressed in between the stripes to an extent that the most significant supercurrent is not in a path meandering around the stripes, but instead is a more direct path toward the edges of the TES.

$I(B)$ for the 5-stripe and no-stripe devices is shown in Fig. 5 at different bath temperatures. This shows the evolution of the smooth Fraunhofer-type pattern observed close to T_c, to the highly distorted pattern seen at lower T_{bath}. In both devices, this distortion appears to occur as different oscillations change in magnitude relative to each other. As these oscillations intersect, abrupt changes in dI/dB, which are shown above to be associated with kinks in $R(T)$, are observed.

$I(B)$ measured at T_{bath} just below T_c for the 3-stripe T-stem device, shown in Fig. 6, has a more complex oscillatory pattern. Consistent with previous observations of devices with relatively sparsely spaced stripes, the measured B_p is larger than the predicted Φ_0/A [2]. There has not yet been a complete theoretical description of this loss of area scaling of the oscillation period in these devices, but one concept is that a complex meandering current distribution is established that leads to weak link or phase-slip behavior in small regions of the TES rather than the device as a whole [2]. If this interpretation is correct, it suggests that in this 3-stripe device a meandering supercurrent path may be significant. Here, we also find that in both $I(B)$ and $I_c(B)$ we observe a small additional peak at the minimum of the central maximum. Given what is shown above for the 5-stripe and no-stripe devices, any theoretical description of these patterns should consider a competition between supercurrent paths meandering around the stripes and directly across the TES. How the various current paths may distort the $I(B)$ pattern, and whether they can account for the additional peak that is observed, remains an open question.

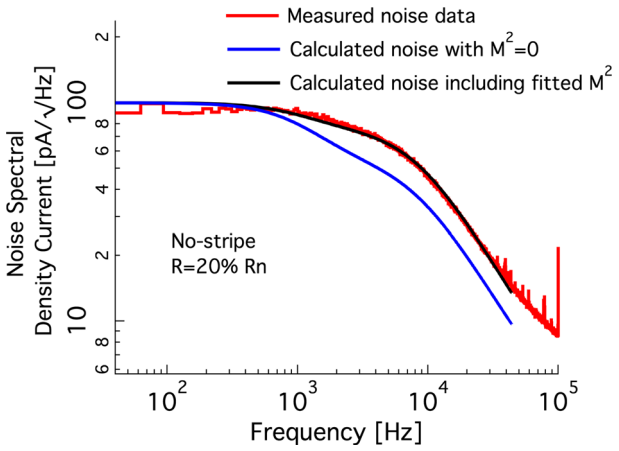

Fig. 7 Measured noise spectral density current (red) for the no-stripe device biased at $R/R_n = 20\%$ as a function of frequency. Calculated noise curves with (black) and without (blue) the fitted contribution of the unexplained noise term M^2 (Color figure online)

3 Spectral Performance of No-Stripe Devices

The relatively smooth $R(T)$ and α_{IV} curves in the no-stripe device indicate that this design may be more robust to small changes in external parameters than the traditional 3-stripe devices, improving the uniformity of performance across a large array. Therefore, we were motivated to more fully characterize the transition properties and spectral performance of the no-stripe device. To achieve this, the impedance of the TES was measured in the range of 10 Hz–5 kHz at various bias points throughout the transition. This was then combined with measurements of the heat capacity $[C(T_c) = 0.97\,\text{pJ/K}]$ and thermal conductance $[G(T_c) = 218\,\text{pW/K}]$ of the pixel (described elsewhere [2,8]), to fit the parameters $\alpha = \frac{T}{R}\frac{\partial R}{\partial T}\Big|_I$ and $\beta = \frac{I}{R}\frac{\partial R}{\partial I}\Big|_T$ at each bias point using the single-body heat capacity model [13] . The noise spectrum of each device was measured at various bias points in the transition. The fitted values of α, β and measured R/R_n were then used to fit measured noise, using the usual expression for the thermal fluctuation noise in the device [8], and the following expression for the voltage noise, $V_n = \sqrt{4k_B RT(1+2\beta)(1+M^2)}$, where k_B is Boltzmann's constant and the unexplained noise is parameterized by M^2. This method is discussed in more detail elsewhere [2,7,13]. Data and calculated noise curves for the no-stripe device at $R/R_n = 20\%$, with and without the fitted M^2 term, are shown in Fig. 7.

Figure 8 shows the fitted values of α, β and M^2 at various values of R/R_n for the no-stripe device measured in this experiment, and these are compared with previous measurements of a 3-stripe T-stem device [2].

In these devices in the limit of strong electro-thermal feedback with a shunt resistance much less than R, the predicted small-signal energy resolution (full width at half maximum) is given by [2,8], $\Delta E \approx 2.355\sqrt{4k_B T^2 C\sqrt{(1+2\beta)(1+M^2)}/\alpha}$. The predicted $\Delta E \approx 1.5$ eV for $R/R_n = 10{-}30\%$ in the no-stripe device. The no-stripe device was used to measure the K_α line of Al at a resolution 1.6 eV, which

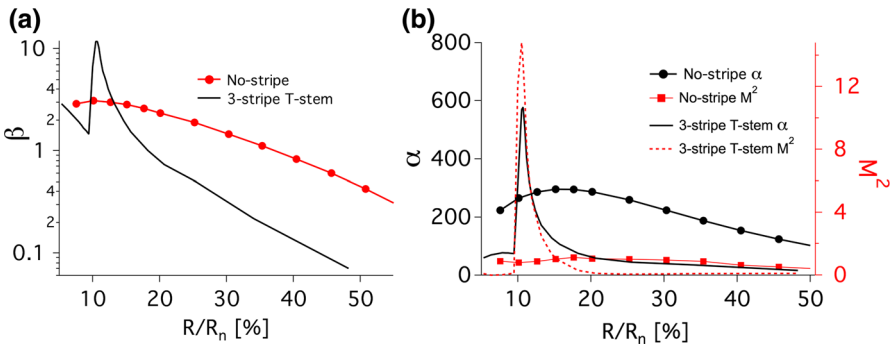

Fig. 8 Comparison of transition parameters of previous data on square 3-stripe T-stem 140 μm TES [2], with data on a no-stripe 140 μm TES from this work. Transition properties, **a** β and **b** α and M^2 for no-stripe and 3-stripe T-stem devices as a function of percentage bias point within the transition. Measured with $T_{\text{bath}} = 55$ mK (Color figure online)

is in reasonable agreement with this predicted small-signal resolution. The larger α in the device with no stripes compared with the 3-striped T-stem device means that for high-energy X-rays the heat capacity of the absorber must be increased to avoid significant degradation of the spectral performance from nonlinearity of the response. With sufficient increase in the heat capacity to limit the current pulse height from a 6 keV photon to that measured in traditional 3-striped devices, we predict an energy resolution in no-stripe devices of $\sim$ 1.9 eV at 6 keV for $R/R_n \approx 15{-}30\%$. This spectral resolution would be comparable to that commonly achieved in the traditional 3-stripe T-stem devices [7].

The prediction of excellent spectral resolution in a device without normal metal stripes is a surprise given results of previous studies, which showed that in devices without stripes the unexplained noise was sufficiently large to significantly degrade the spectral resolution [4,14]. Previous measurements of 250 μm devices with no stripes had $\alpha \sim 250$ and $M^2 \sim 35{-}50$ [14]. In the 140 μm no-stripe devices measured in this work, we find $\alpha \sim 250$ but $M^2 \sim 1$. The significantly reduced unexplained noise term is the reason for the prediction of better energy resolution in 140 μm devices. The explanation and robustness of this apparent difference will need to be investigated thoroughly in the future. It may be a consequence of the different sizes of the devices, or it may be the result of more subtle differences between the devices.

4 Conclusion

In conclusion, we have shown that changes to the normal metal stripes added on top of a TES can have dramatic effects on the appearance of localized kinks commonly observed in the resistive transition. We have correlated these changes to changes in the oscillatory pattern of $I(B)$, which we interpreted as resulting from changes in the supercurrent distribution within the TES. TESs without stripes show a broad region of parameter space without kinks, which is desirable for achieving uniformity of performance across a large array of devices, and achieving the energy gain scale

calibration requirements for Athena [3]. Initial measurements and calculations suggest that the spectral performance of the devices without stripes may be comparable to the traditional striped devices.

References

1. L. Ravera et al., Proc. SPIE **9144**, 13 (2014). https://doi.org/10.1117/12.2055884
2. S. Smith et al., J. Appl. Phys. **114**, 074513 (2013). https://doi.org/10.1063/1.4818917
3. Athena Calibration Requirements Issue 0.3. Feb 8, 2017. Document: ESA-ATH-SP-2016-001
4. J. Ullom et al., Appl. Phys. Lett. **84**, 4206 (2004). https://doi.org/10.1063/1.1753058
5. M. Lindeman et al., Nucl. Instr. Meth. Phys. Res. A **520**, 348 (2004). https://doi.org/10.1016/j.nima.2003.11.264
6. J. Sadleir et al., Phys. Rev. B **84**, 184502 (2011). https://doi.org/10.1103/PhysRevB.84.184502
7. N. Iyomoto et al., J. Low Temp. Phys. **151**, 406 (2008). https://doi.org/10.1007/s10909-007-9668-3
8. K.D. Irwin, G.C. Hilton, *Cryogenic Particle Detection*, vol. 99 (Springer, Berlin, 2005). Ch. 3
9. J. Sadleir et al., Phys. Rev. Lett. **104**, 047003 (2010). https://doi.org/10.1103/PhysRevLett.104.047003
10. J. Ullom, D. Bennett, Supercond. Sci. Technol. **28**, 084003 (2015)
11. M. Tinkham, *Introduction to Superconductivity*, 2nd edn. (McGraw-Hill, New York, 1996)
12. J. E. Sadleir, Ph.D. Thesis, University of Illinois (2010)
13. N. Iyomoto et al., Appl. Phys. Lett. **92**, 013508 (2008). https://doi.org/10.1063/1.2830665
14. N. Jethava et al., AIP Conf. Proc. **1185**, 31 (2009). https://doi.org/10.1063/1.3292343